Supporting Information

Intrinsic Defect-rich Graphene Coupled Cobalt Phthalocyanine for Robust Electrochemical Reduction of Carbon Dioxide

Fengxia Liang, Jun Zhang, Zewei Hu, Chao Ma, Wenpeng Ni*, Yan Zhang*, and Shiguo Zhang*

College of Materials Science and Engineering, Hunan Province Key Laboratory for Advanced Carbon Materials and Applied Technology, Hunan University, Changsha 410004, China

Corresponding author: * E-mail: Wenpeng Ni, aniwenpeng@163.com;

Yan Zhang, zyan1980@hnu.edu.cn;

Shiguo Zhang, zhangsg@hnu.edu.cn

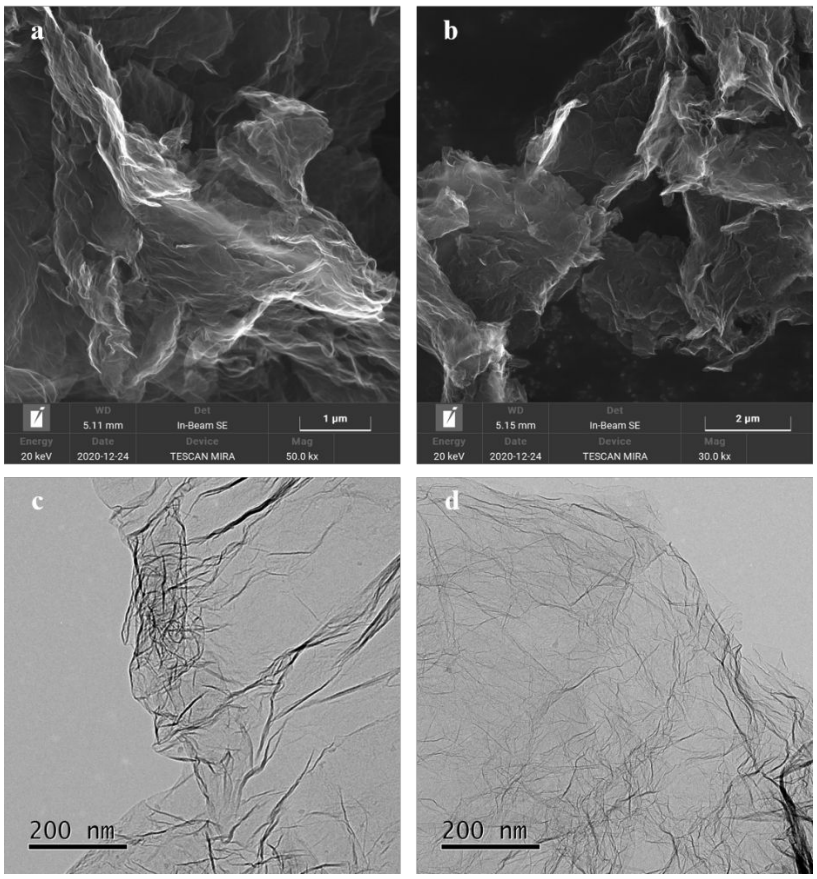

Figure S1. SEM images of (a) rGO, and (b) DrGO. TEM images of (c) rGO, and (d) DrGO.

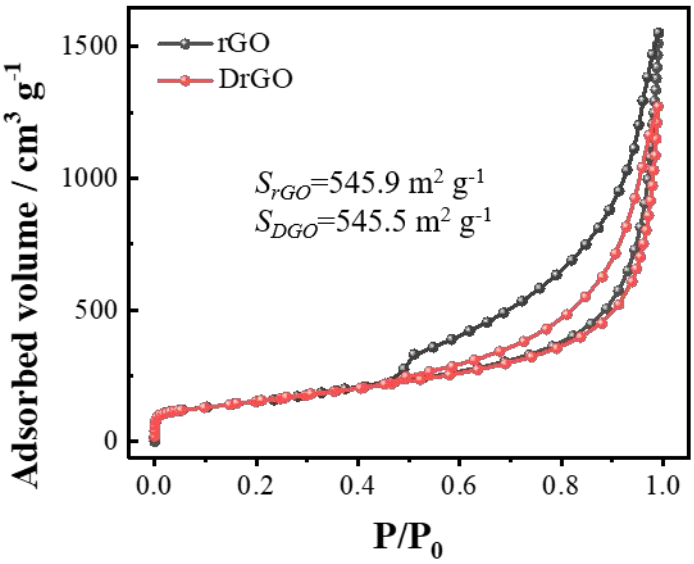

Figure S2. N_2 adsorption-desorption curves of rGO and DrGO.

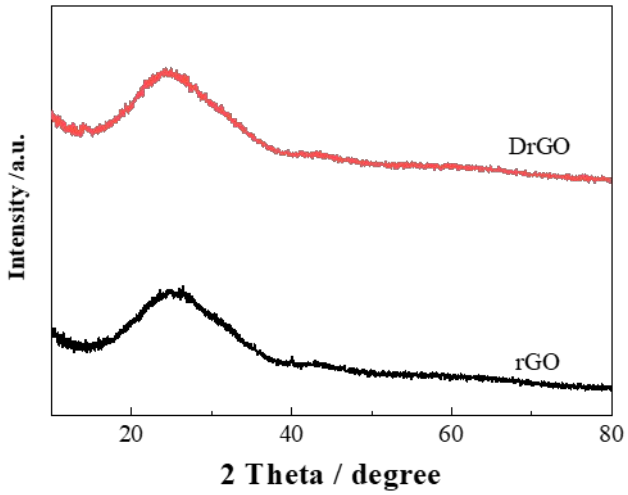

Figure S3. XRD patterns of rGO and DrGO.

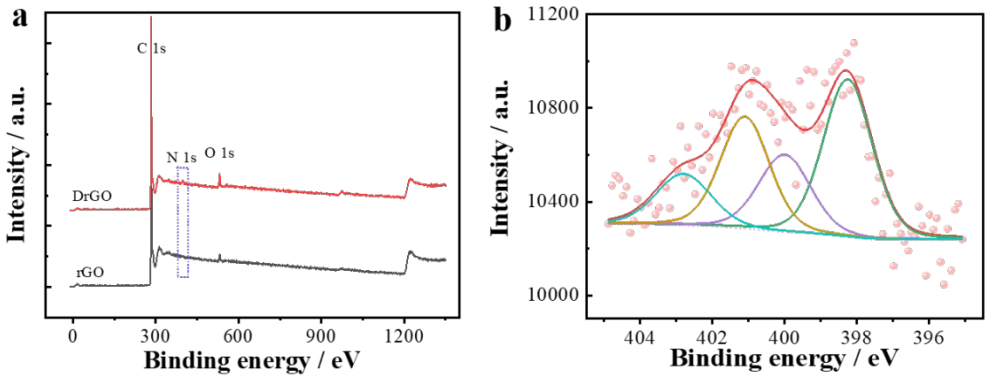

Figure S4. (a) The XPS full spectrum of rGO and DrGO. (b) High-resolution XPS N 1s spectrum of DrGO.

Table S1. The content of C, O, N, and Co elements in rGO, DrGO, rGO-CoPc, and DrGO-CoPc collected by XPS spectra.

	C / at.%	O / at.%	N / at.%	Co / at.%	Co / wt.%
rGO	97.25	2.76	NA	NA	NA
DrGO	94.88	3.49	1.64	NA	NA
rGO-CoPc	93.87	3.11	2.64	0.39	1.39
DrGO-CoPc	94.12	2.45	3.1	0.33	1.35

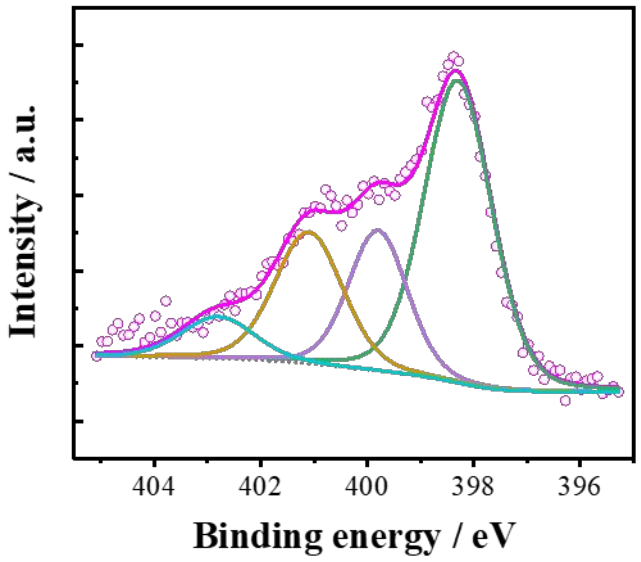

Figure S5. High-resolution XPS N 1s spectrum of NrGO-750.

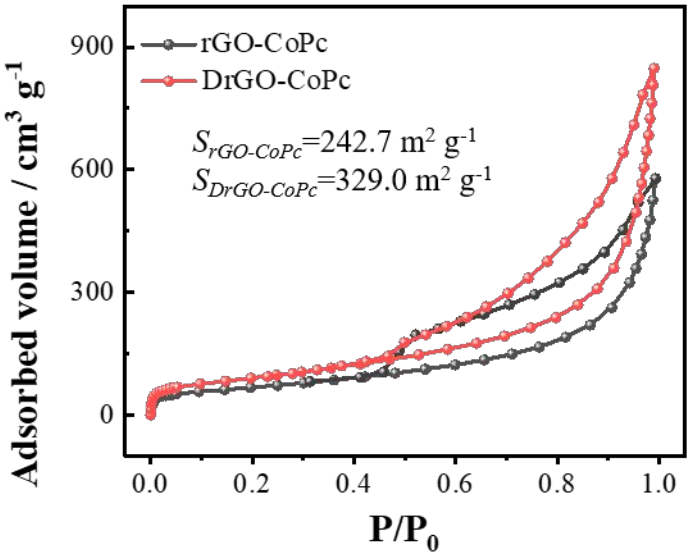

Figure S6. N_2 adsorption-desorption curves of rGO-CoPc and DrGO-CoPc.

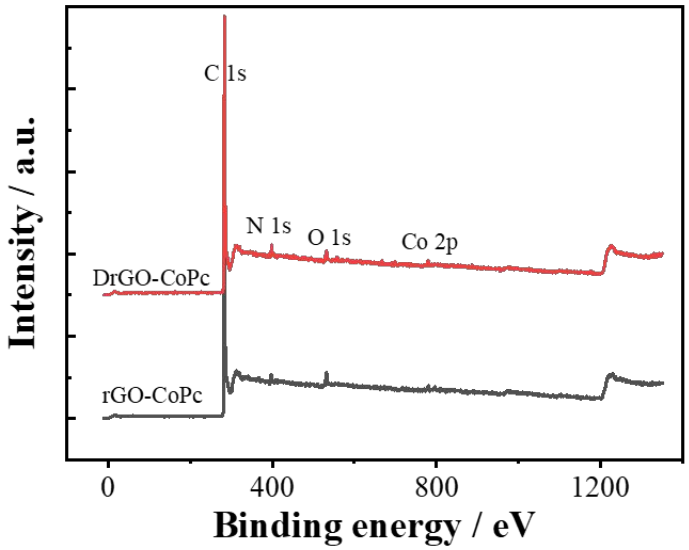

Figure S7. The XPS full spectrum of rGO-CoPc and DrGO-CoPc.

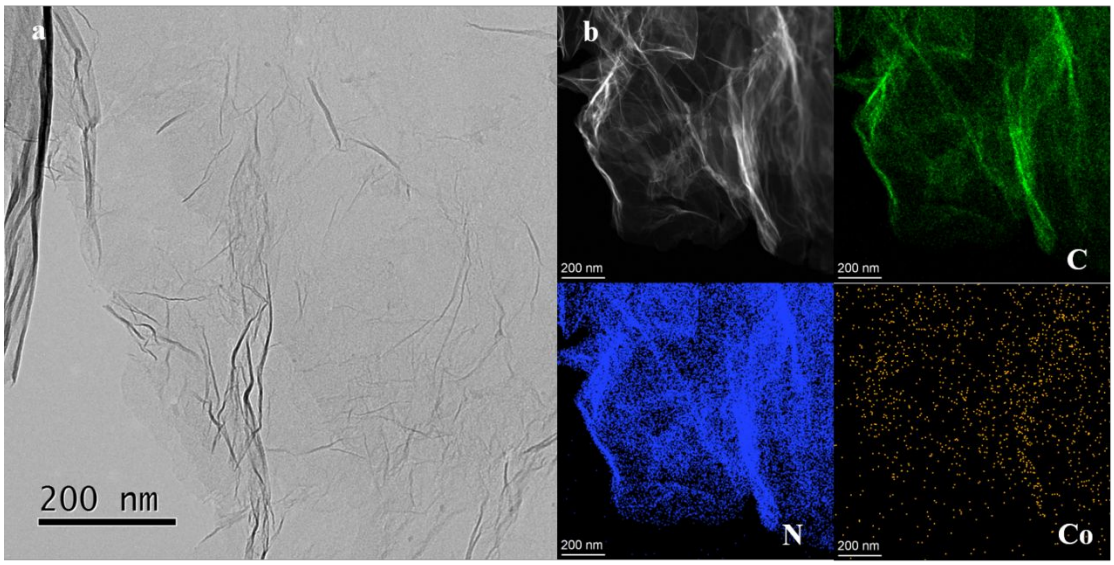

Figure S8. (a) TEM image, and (b) EDX mapping (C, N, and Co element) of rGO-CoPc.

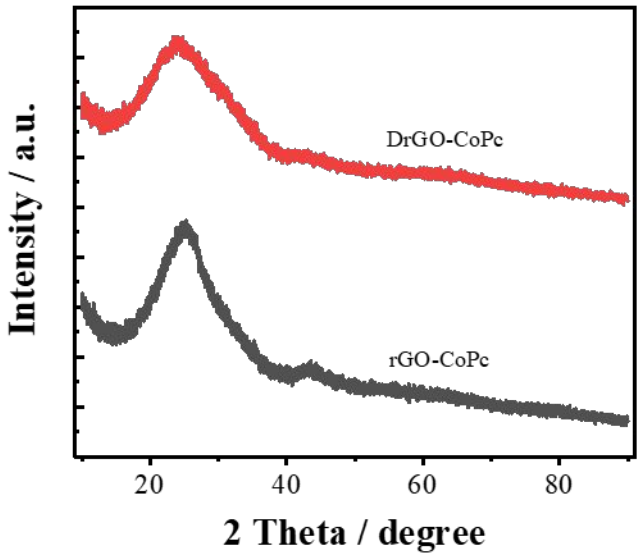

Figure S9. XRD patterns of rGO-CoPc and DrGO-CoPc.

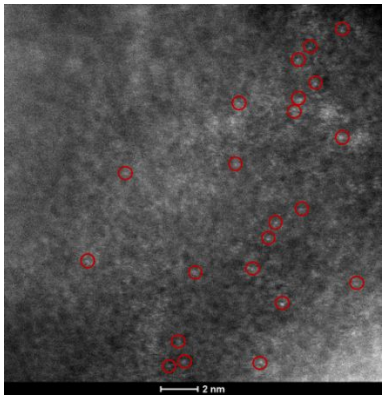

Figure S10. AC HAADF-STEM image of rGO-CoPc.

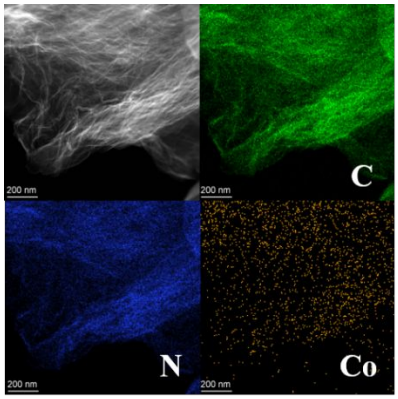

Figure S11. EDX mapping (C, N, and Co element) of DrGO-CoPc.

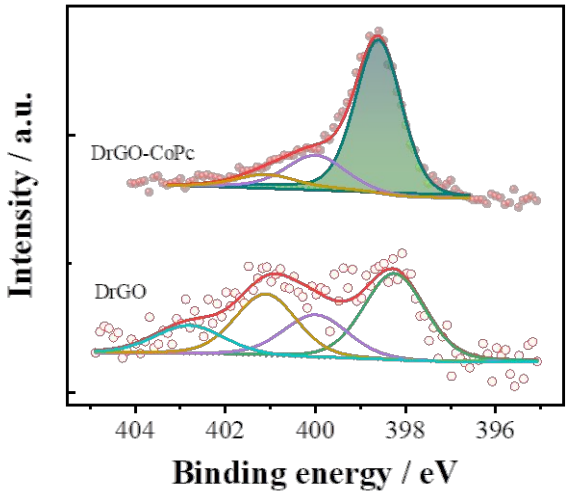

Figure S12. High resolution XPS N 1s spectra of DrGO and DrGO-CoPc.

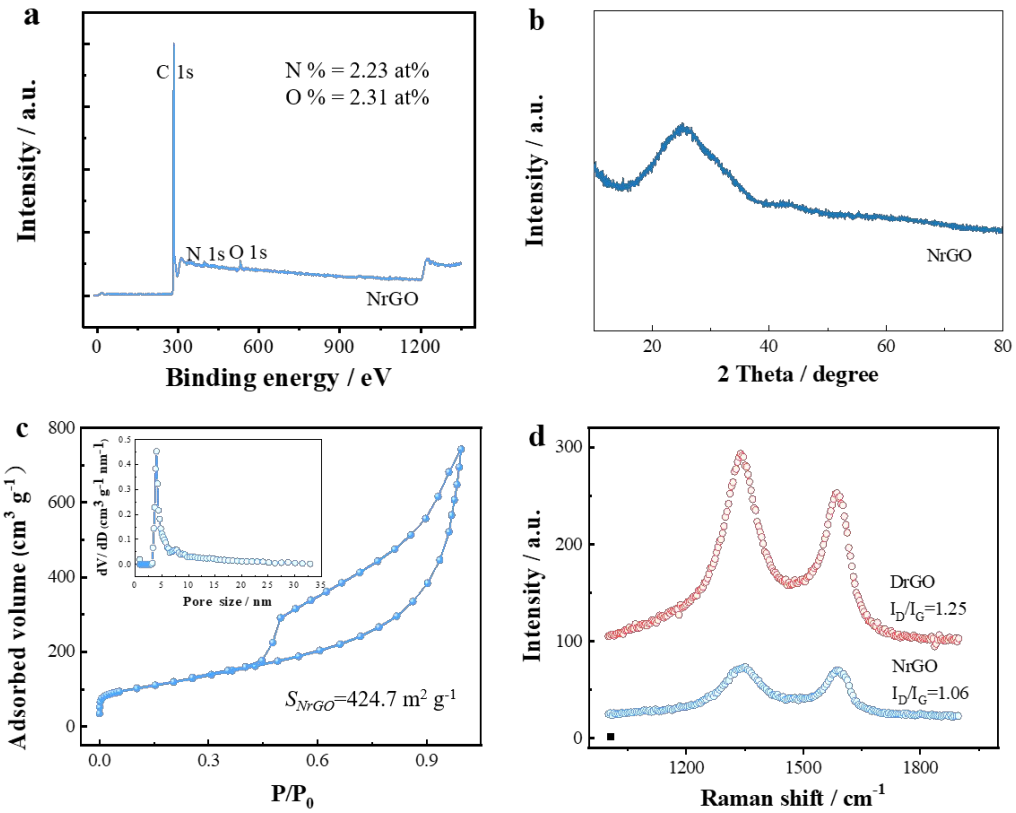

Figure S13. (a) XPS full spectra, (b) XRD pattern, and (c) N_2 adsorption-desorption curve of NrGO. (d) Raman spectra of NrGO and DrGO.

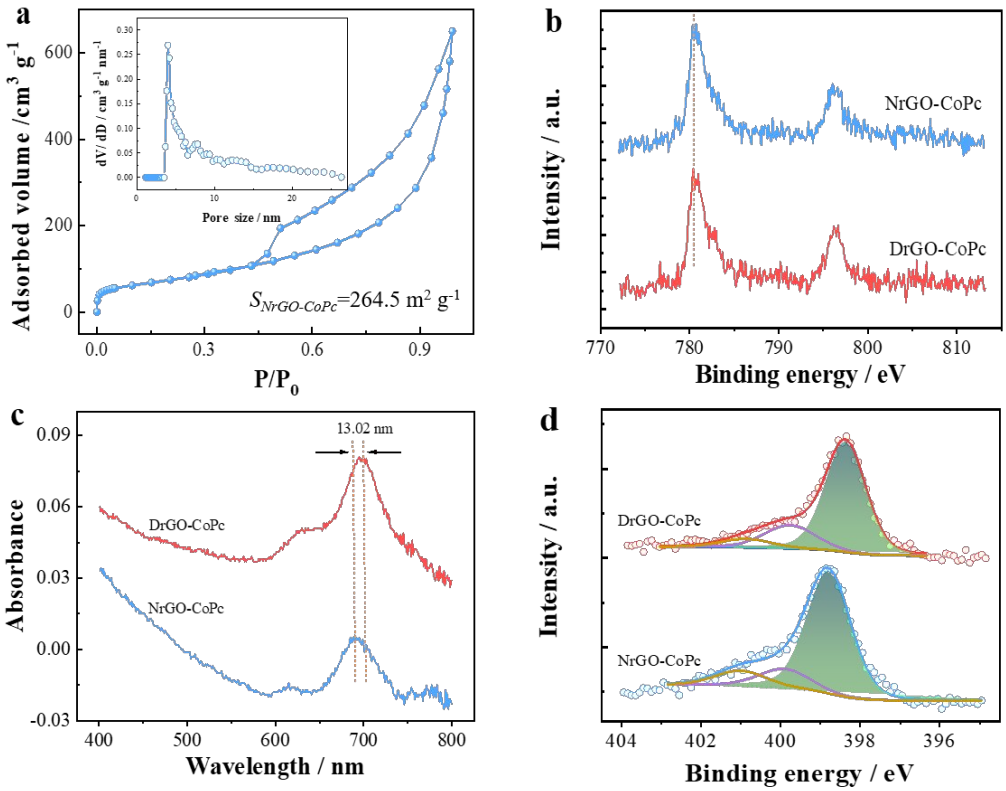

Figure S14. (a) N_2 adsorption-desorption curve of NrGO-CoPc. (b) High resolution XPS Co 2p spectra, (c) UV-vis spectra, and (d) XPS N 1s spectra of DrGO-CoPc and NrGO-CoPc.

The largest shift of the peak for inner core nitrogen atoms could be ascribed to the stronger electron communication between CoPc and DrGO. If the N 1s spectra shift is caused by the simple spectra mixture of graphene matrix and CoPc, the NrGO-CoPc should has comparable or larger negative shift than DrGO-CoPc due to the higher content of total N atoms in NrGO (2.23% vs 1.64%). However, as shown in Figure S14d, the peak for the inner core nitrogen atoms located at 398.9 eV in the N 1s spectrum of NrGO-CoPc, giving the lower peak shift than that of DrGO-CoPc. Therefore, we think the spectra mixture of graphene matrix and CoPc is not the contribution to the peak shift for the inner core nitrogen atoms. Moreover, the peak shift was also observed in the N 1s spectrum of rGO-CoPc (**Figure 2d**), wherein rGO is a matrix without N dopants. Such shift illustrates that the electron communication could induce the N 1s spectra shift. Therefore, it could be concluded that the peak shift is caused by the interaction between CoPc and DrGO.

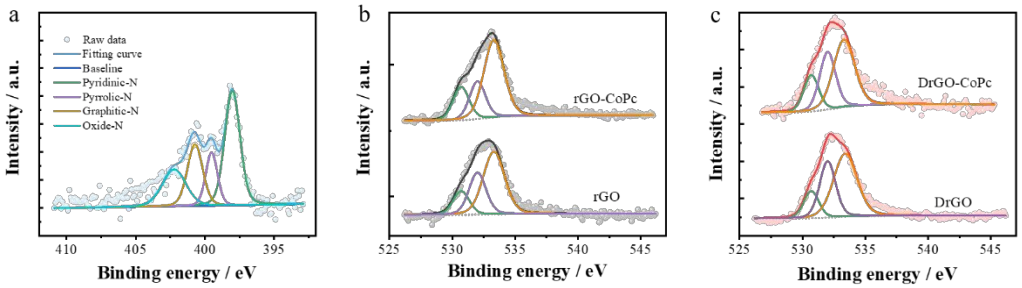

Figure S15. (a) High-resolution N 1s XPS spectrum of NrGO. High-resolution O 1s XPS of (b) rGO and rGO-CoPc, and (c) DrGO and DrGO-CoPc.

As for N dopants, the high-resolution N 1s XPS spectrum of DrGO could be deconvoluted into pyridinic-N, pyrrolic-N, graphitic-N, and oxidized-N with the fraction of 40.2%, 14.2%, 25.4%, and 20.2%, respectively. For comparison, the N dopant in NrGO was also analyzed by XPS, giving total N content of 2.23at%, which is slightly higher than that of DrGO (1.64at%). The percentage of pyridinic-N, pyrrolic-N, graphitic-N, and oxidized-N are 37.4%, 21.7%, 27.3%, and 13.6%, respectively.

As for O elements, the O-containing groups can interact with Co ion in CoPc by ligand-like interaction or axial coordination. Carboxyl and hydroxy groups are the two potential anchoring sites for CoPc via forming axial Co-O bond. Notably, such direct interaction will induce positive shift of the XPS peak of oxygen-functional groups. However, there is no distinct shift of the binding energy of O 1s peak for both rGO and DrGO after supporting CoPc (Fig. S15b and S15c), implying that CoPc is not directly coordinated with O-containing groups in this work. This is not unexpected because carboxylic, hydroxy, and ether groups with poor thermal stability are likely to be removed during high temperature (1000 °C) reduction. The fitting of the high-resolution O 1s XPS spectra delivers that the C=O (532.0 eV) and C-O (533.3 eV) are the main oxygen-functional groups in all samples (Fig. S15b and S15c). The lack of the carboxyl and hydroxy groups that can coordinate with CoPc may exclude the direct interaction of O-containing group with CoPc in this work. In fact, Co ions bearing four N coordination atoms possesses very weak interaction with O-containing groups in graphene.

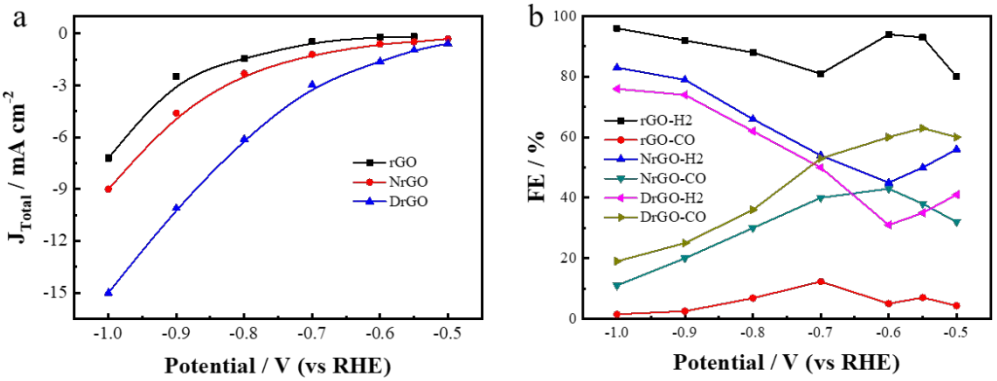

Figure S16. (a) J_{Total}, and (b) FE of CO and H_2 for rGO, NrGO, and DrGO.

Table S2. Summary of the electrochemical performance of DrGO-CoPc and other heterogeneous molecular catalysts.

Catalysts	Electrolyte	Potential (vs. RHE)	FE	J_{CO} (mA/cm^2)	Ref
DrGO-CoPc	0.1 M $KHCO_3$	-0.78 V	91%	-29.8	This work
CoP@NrGO	0.5 M $NaHCO_3$	-0.8 V	87%	-4	1
CoPc/CNT	0.1 M $KHCO_3$	-0.8 V	80%	-10	2
CCG/CoPc-A	0.1 M $KHCO_3$	-0.8 V	81%	-9	3
CoPPc@g-C_3N_4–CNTs	0.5 M $KHCO_3$	-0.8 V	92%	-21	4
CoPc-CN/CNT	0.1 M $KHCO_3$	-0.63 V	98%	-15	5
CoPPc/CNT	0.5 M $NaHCO_3$	-0.61 V	>90%	-20	6
CoPc/CNT	0.1 M $KHCO_3$	-0.61 V	>90%	-10	7
CoPc-py-CNT	0.1 M $NaHCO_3$	-0.63 V	98%	-6	8
FePc-Gr75	0.1 M $KHCO_3$	-0.7 V	80%	-1.9	9
CoPc1MWCNTs	0.5 M $NaHCO_3$	-0.68 V	91%	-14	10
NiPc–OMe MDE	0.5 M $KHCO_3$	-0.60 V	99.5%	-32	11
NapCo@SNG	0.1 M $KHCO_3$	-0.8 V	97%	-2	12
CoPPc-CNT	0.5 M $NaHCO_3$	-0.7 V	95%	-8	13
CoTPP/CNT	0.5 M $KHCO_3$	-1.15 V vs. SCE	83%	-0.59	14
CoPc/CWM	0.1 M $KHCO_3$	-0.78 V	90%	-4.58	15
CoPc-py-CNT	0.5 M $KHCO_3$	-0.6 V	95%	-6.8	16
PyNiPc/CNT	0.5 M $KHCO_3$	-0.8 V	>95%	-20	17
Co@Pc/C	0.5 M $KHCO_3$	-0.9 V	84 %	-28	18
CoOx/FePc	0.5 M $KHCO_3$	-0.7 V	83%	-24	19
CoFPc	0.5 M $NaHCO_3$	-0.8 V	92%	-4.2	20
CoII(Ch)/MWCNTs	5.0 mM Na_2SO_4	-1.1 V	89%	/	21
[MnBr(2,2′-bipyridine)$(CO)_3$]	0.5 M $KHCO_3$	-1.1 V vs. SHE	46 μmol/cm^2	-5	22
CuPc	0.5 M $KHCO_3$	-1.06 V	66% CH_4	-13	23
$[Co(qpy)]_2$+@MWCNTs	0.5 M $NaHCO_3$	-0.48 V	100%	-10	24
CoPc/CNT	0.1 M $KHCO_3$	-0.82 V	44%	-10.6	25
AgDAT/C	1 M KOH	-1.4 V vs. Ag/AgCl	85%	-10	26
CoPc-P4VP	0.1 M NaH_2PO_4	-0.73 V	90%	-2	27
CATPyr	0.5 M $NaHCO_3$	-1.03 V vs. NHE	97%	/	28
CATCO2H	0.5 M $NaHCO_3$	-1.06 V	90%	/	29

		vs. SHE			
PorZn	0.1M $TBAPF_6$ DMF/H_2O	-1.7 V vs. SHE	95%	-2.5	30
$Fe_2DTPFPP\text{-}PO_3H_2$	DMF/H_2O/0.1 M $TBAPF_6$	-1.2 V	93%	/	31
CoPP	0.5 M K_2SO_4	-1.3 V vs. Ag/AgCl	84%	/	32
CoTMPP/ACF	0.5 M $KHCO_3$	-1.45 V vs. SCE	85%	50	33
CuPolyPc@CNT	0.1 M $CsHCO_3$	-0.7 V	80%	> 7	34
CoPc	0.1 M $KHCO_3$	-0.8 V	99%	-3.2	35

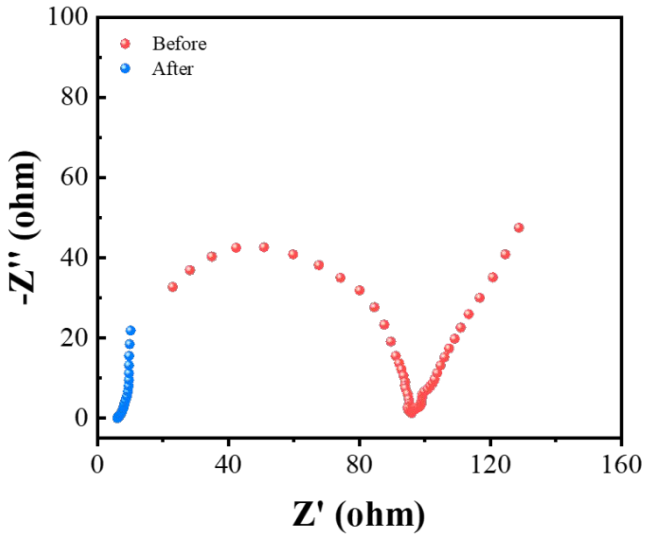

Figure S17. Nyquist plots for DrGO-CoPc before and after durability test.

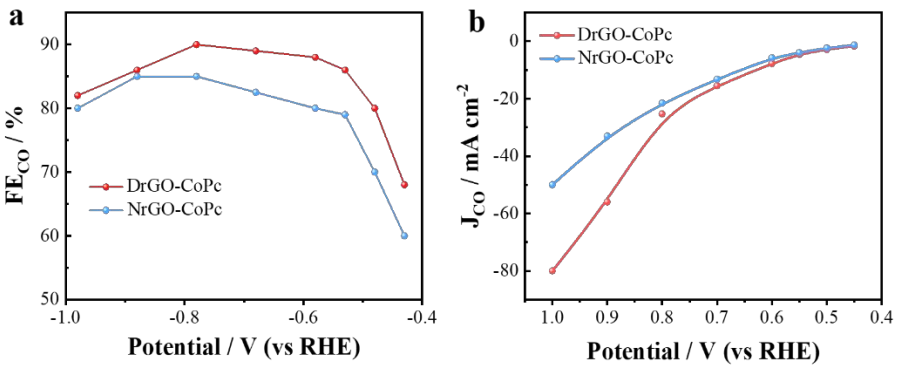

Figure S18. (a) FE_{CO}, (b) J_{CO} of DrGO-CoPc and NrGO-CoPc.

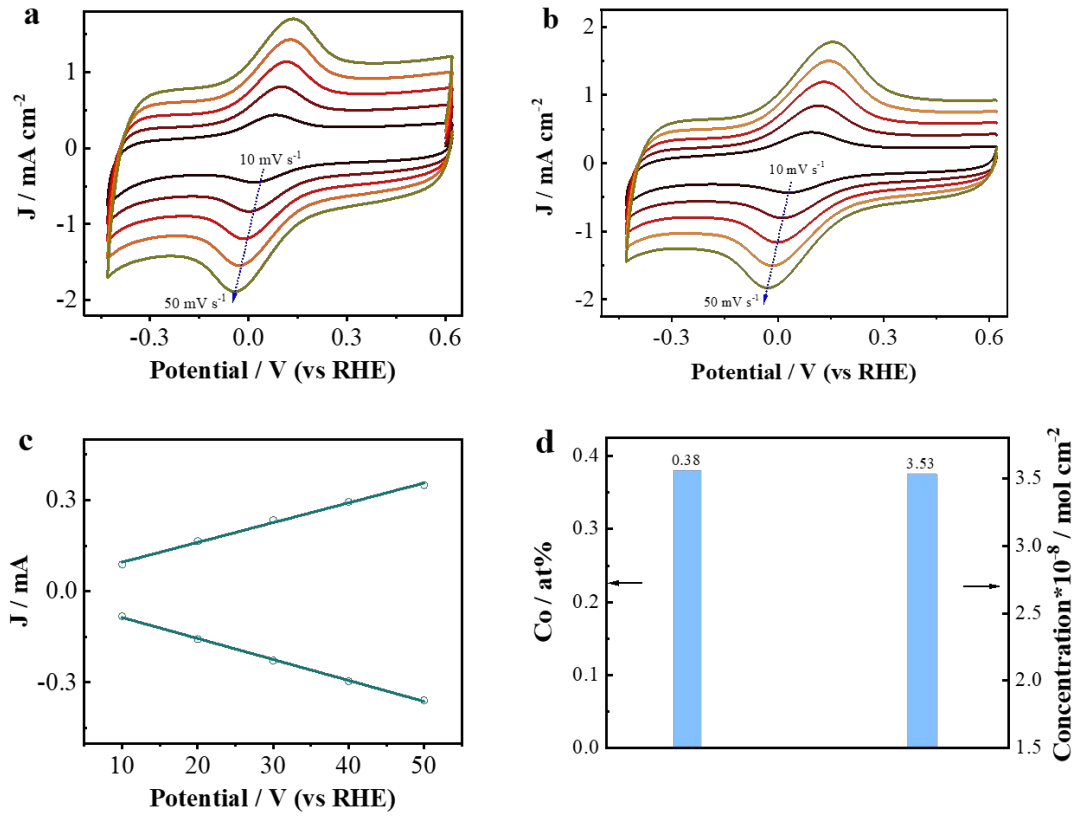

Figure S19. Co^{2+}/Co^{+} redox curves of (a)rGO-CoPc and (b) NrGO-CoPc recorded with the scan rate from 10 mV s^{-1} to 50 mV s^{-1}. (c) The plot of the anodic and cathodic peak current densities of Co^{2+}/Co^{+} redox peak versus the scan rate. (d) The content of Co atom collected by XPS test and the concentration of electrochemical active Co sites in NrGO-CoPc.

The coverage of electrochemical active Co site (Γ) was further calculated by the equation as following.

$i_{p,c} = (n^2F^2\nu A\Gamma)/(4RT)$ (1)

Where n is the number of electrons transferred (n=1 for the redox peak of Co^{2+}/Co^{+}), F is faraday constant (96485 C mol^{-1}), ν is scan rate, A is electrode area, R is gas constant (8.314 J mol^{-1} k^{-1}), T is the temperature (298 K).

Take the DrGO-CoPc as the example, the calculation was conducted as below.

$$\frac{i_{p,c}}{\nu} = \frac{n^2F^2A\Gamma}{4RT} = 0.0088 \text{ mA mV}^{-1} \text{ s} \quad (2)$$

$$0.0088 \text{ mA mV}^{-1} \text{ s} = \frac{1^2 \times 96485^2 \times \text{A}^2 \text{ s}^2 (\text{mol}^{-1})^2 \times 0.196 \text{ cm}^2 \times \Gamma}{4 \times 8.314 \text{ J mol}^{-1} \text{ K}^{-1} \times 298 \text{ K}} \quad (3)$$

$$\Gamma = \frac{0.0088 \text{ A V}^{-1} \text{ s} \times 4 \times 8.314 \text{ V A s} \times 298}{964852 \times \text{A}^2 \text{ s}^2 \text{ mol}^{-1} \times 0.196 \text{ cm}^2} \quad (4)$$

$$\Gamma = \frac{0.0088 \times 4 \times 8.314 \times 298}{964852 \times \text{mol}^{-1} \times 0.196 \text{ cm}^2} = 4.78 \times 10^{-8} \text{ mol cm}^{-2} \quad (5)$$

Table S3. The fitting results of Nyquist plots of rGO-CoPc and DrGO-CoPc.

	Rs / Ω	Rct / Ω
rGO-CoPc	10.15	106.30
DrGO-CoPc	7.84	83.39

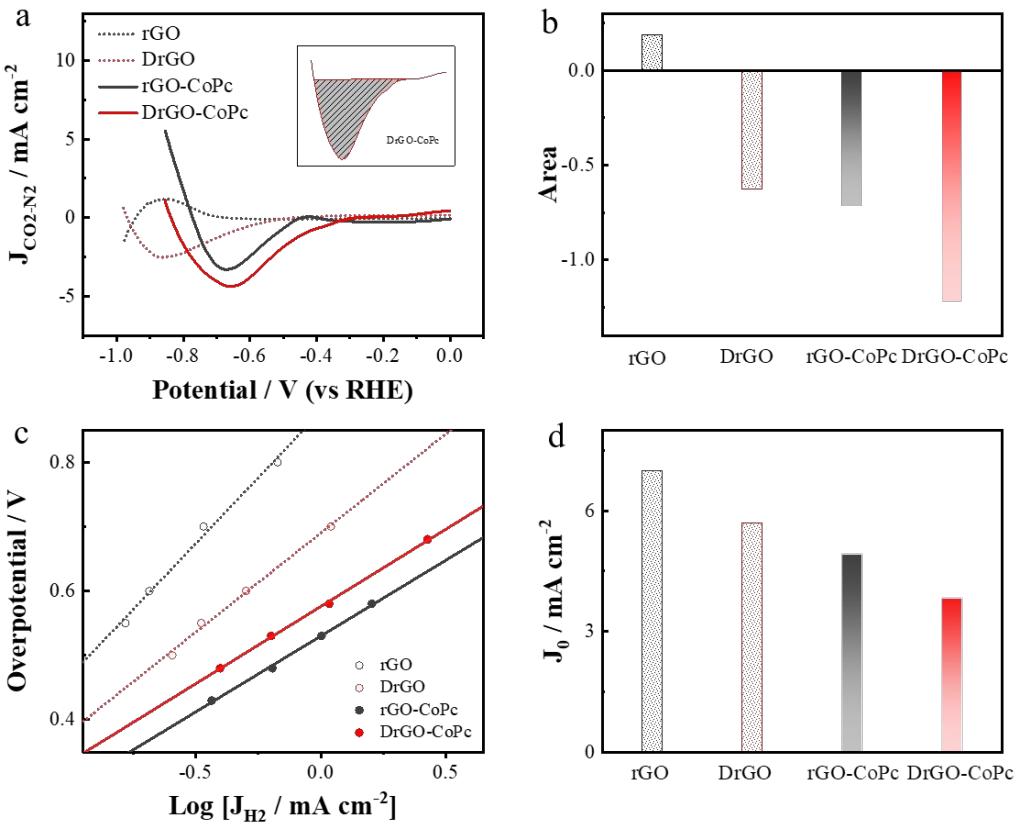

Figure S20. (a) Polarization curves of pure CO_2 reduction reaction by subtracting the curves collected in N_2-saturated electrolyte from that in CO_2, (b) The integral area of the CO_2 reduction peak, (c) Tafel analysis of the hydrogen evolution, (d) Exchange current density for hydrogen evolution, for rGO, DrGO, rGO-CoPc, and DrGO-CoPc.

Due to the H_2 and CO are the only two reduction products detected by on-line GC with the total FE approaching 100%, the excellent CO selectivity of DrGO-CoPc is ascribed to its preferential CO_2RR over the competed hydrogen evolution reaction (HER). We collected the linear sweep voltammetry (LSV) of rGO, DrGO, rGO-CoPc, and DrGO-CoPc in N_2- and CO_2-saturated electrolyte. As confirmed by the GC measurement, the reduction product in the N_2-saturated 0.1 M $KHCO_3$ is exclusively H_2 (Fig. S22), the current density is only attributed to the HER. Therefore,

Therefore, the LSV curves collected in CO_2-saturated electrolyte were subtracted by those collected in N_2-saturated electrolyte, which results in the polarization curves of pure CO_2RR (the pH effect was corrected, Fig. S20a). It can be found that DrGO, rGO-CoPc, and DrGO-CoPc exhibit obvious differential current densities (J_{CO2-N2}). To compare the CO_2RR activity quantitatively, the integral areas of reduction peaks were analyzed, as demonstrated in the inset of Fig. S20a. DrGO-CoPc has the maximal peak area followed by rGO-CoPc and DrGO, meaning that the preferential CO_2RR over HER gives the excellent CO selectivity of DrGO-CoPc.

The HER intrinsic activity of rGO, DrGO, rGO-CoPc, and DrGO-CoPc was compared by analyzing the Tafel plots for HER (Fig. S20c), then calculating the exchange current density at the thermodynamic redox potential (J_0). As summarized in Fig. S20d, DrGO-CoPc has the lowest J_0, suggesting the poorest HER activity. The inferior HER activity of DrGO-CoPc is partly derived from the inherent electronic structure of CoPc. Moreover, the adsorption of CO_2 reduction intermediate tends to reduce the coverage of H*, leading to suppressed HER activity. In addition, the CO_2RR will create an alkaline electrode-electrolyte interface and in turn suppress the competed HER, especially under high current densities. Combining with its enhanced intrinsic activity of CO_2RR, the DrGO-CoPc could give the best CO selectivity.

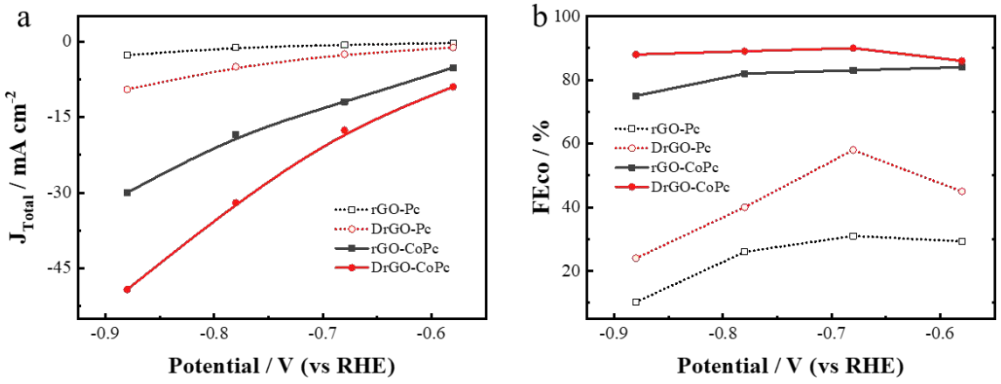

Figure S21. (a) Total current density, and (b) FE_{CO} of rGO-Pc, DrGO-Pc, rGO-CoPc, and DrGO-CoPc.

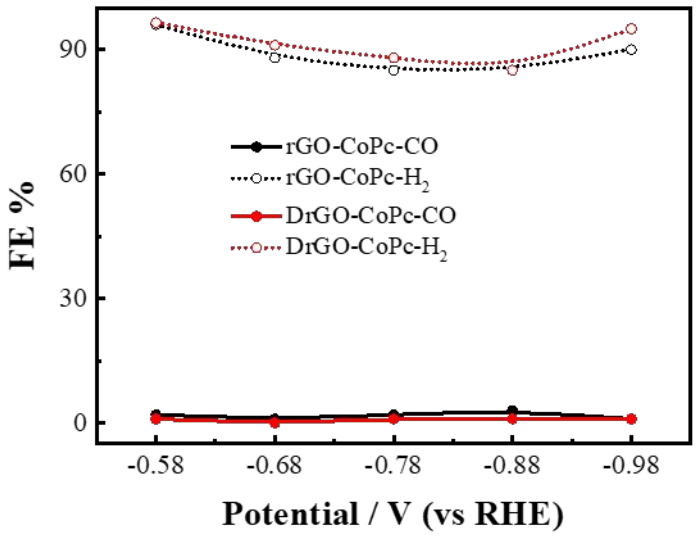

Figure S22. Faradaic efficiency of H_2 and CO of rGO-CoPc and DrGO-CoPc collected in N_2 saturated electrolyte.

References

1. Zhu, M; Cao, C; Chen, J; Sun, Y; Ye, R; Xu, J; Han, Y-F. Electronic Tuning of Cobalt Porphyrins Immobilized on Nitrogen-Doped Graphene for CO_2 Reduction. *ACS Appl. Energy Mater.*, **2019**, *2*, 2435-2440.
2. Huai, M. M; Yin, Z. L; Wei, F. Y; Wang, G. W; Xiao, L; Tu, J. T; Zhuang, L. Electrochemical CO_2 Reduction on Heterogeneous Cobalt Phthalocyanine Catalysts with Different Carbon Supports. *Chem. Phys. Lett.*, **2020**, *754*, 137655-137659.
3. Choi, J; Wagner, P; Gambhir, S; Jalili, R; MacFarlane, D. R; Wallace, G. G; Officer, D. L. Steric Modification of a Cobalt Phthalocyanine/Graphene Catalyst To Give Enhanced and Stable Electrochemical CO_2 Reduction to CO. *ACS Energy Lett.*, **2019**, *4*, 666-672.
4. Li, T. T; Mei, Y; Li, H. W; Qian, J. J; Wu, M; Zheng, Y. Q. Highly Selective and Active Electrochemical Reduction of CO_2 to CO on a Polymeric Co(II) Phthalocyanine@Graphitic Carbon Nitride Nanosheet-Catbon Nanotube Composite. *Inorg. Chem.*, **2020**, *59*, 14184-14192.
5. Zhang, X; Wu, Z. S; Zhang, X; Li, L. W; Li, Y. Y; Xu, H. M; Li, X. X; Yu, X. L; Zhang, Z. S; Liang, Y. Y; Wang, H. L. Highly Selective and Active CO_2 Reduction Electrocatalysts Based on Cobalt Phthalocyanine/Carbon Nanotube Hybrid Structures. *Nat. Commun.*, **2017**, *8*, 14675-14682.
6. Han, N; Wang, Y; Ma, L; Wen, J. G; Li, J; Zheng, H. C; Nie, K. Q; Wang, X. X; Zhao, F. P; Li, Y. F; Fan, J; Zhong, J; Wu, T. P; Miller, D. J; Lu, J; Lee, S. T; Li, Y. G. Supported Cobalt Polyphthalocyanine for High-performance Electrocatalytic CO_2 Reduction. *Chem*, **2017**, *3*, 652-664.
7. Jiang, Z; Wang, Y; Zhang, X; Zheng, H. Z; Wang, X. J; Liang, Y. Y. Revealing the Hidden Performance of Metal Phthalocyanines for CO_2 Reduction Electrocatalysis by Hybridization with Carbon Nanotubes. *Nano Res.*, **2019**, *12*, 2330-2334.

8. Zhu, M. H; Chen, J. C; Guo, R; Xu, J; Fang, X. C; Han, Y. F. Cobalt Phthalocyanine Coordinated to Pyridine-functionalized Carbon Nanotubes with Enhanced CO_2 Eelctroreduction. *Appl. Catal. B: Environ.*, **2019**, *251*, 112-118.
9. Li, X. X; Chai, G. L; Xu, X; Liu, J. J; Zhong, Z; Cao, A. H; Tao, Z. J; You, W. F; Kang, L. T. Electrocatalytic Reduction of CO_2 to CO over Iron Phthalocyanine-modified Graphene Nanocomposites. *Carbon*, **2020**, *167*, 658-667.
10. Wang, M; Torbensen, K; Salvatore, D; Ren, S. X; Joulie, D; Dumoulin, F; Mendoza, D; Lassalle-Kaiser, B; Isci, U; Berlinguette, C. P; Robert, M. CO_2 Electrochemical Catalytic Reduction with a Highly Active Cobalt Phthalocyanine. *Nat. Commun.*, **2019**, *10*, 3602-3609.
11. Zhang, X; Wang, Y; Gu, M; Wang, M. Y; Zhang, Z. S; Pan, W. Y; Jiang, Z; Zheng, H. Z; Lucero, M; Wang, H. L; Sterbinsky, G. E; Ma, Q; Wang, Y. G; Feng, Z. X; Li, J; Dai, H. J; Liang, Y. Y. Molecular Engineering of Dispersed Nickel Phthalocyanines on Carbon Nanotubes for Selective CO_2 Reduction. *Nat. Energy*, **2020**, *5*, 684-692.
12. Wang, J; Huang, X; Xi, S. B; Lee, J. M; Wang, C; Du, Y. H; Wang, X. Linkage Effect in the Heterogenization of Cobalt Complexes by Doped Graphene for Electrocatalytic CO_2 Reduction. *Angew. Chem. Int. Ed.*, **2019**, *58*, 13532-13539.
13. Chen, J. C; Li, J. Y; Liu, W. L; Ma, X. H; Xu, J; Zhu, M. H; Han, Y. F. Facile Synthesis of Polymerized Cobalt Phthalocyanines for Highly Efficient CO_2 Reduction. *Green Chem.*, **2019**, *21*, 6056-6061.
14. Hu, X. M; Ronne, M. H; Pedersen, S. U; Skrydstrup, T; Daasbjerg, K. Enhanced Catalytic Activity of Cobalt Porphyrin in CO_2 Electroreduction upon Immobilization on Carbon Materials. *Angew. Chem. Int. Ed.*, **2017**, *56*, 6468-6472.
15. Zhang, H. D; Min, S. X; Wang, F; Zhang, Z. G. Immobilizing Cobalt Phthalocyanine into a Porous Carbonized Wood Membrane as a Self-supported Heterogeneous Electrode for Selective and Stable CO_2 Electroreduction in Water. *Dalton Trans.*, **2020**, *49*, 15607-15611.
16. Chen, J. C; Zhu, M. H; Li, J. Y; Xu, J; Han, Y. F. Structure-Activity Relationship of the Polymerized Cobalt Phthalocyanines for Electrocatalytic Carbon Dioxide Reduction. *J. Phys. Chem. C*, **2020**, *124*, 16501-16507.
17. Ma, D. D; Han, S. G; Cao, C. S; Li, X. F; Wu, X. T; Zhu, Q. L. Remarable Electrocatalytic CO2 Reduction with Ultrahigh CO/H_2 Ratio over Single-molecularly Immobilized Pyrrolidinonyl Nickel Phthalocyanine. *Appl. Catal. B: Environ.*, **2020**, *264*, 118530-118537.
18. He, C; Zhang, Y; Zhang, Y. F; Zhao, L; Yuan, L. P; Zhang, J. N; Ma, J. M; Hu, J. S. Molecular Evidence for Metallic Cobalt Boosting CO_2 Electroreduction on Pyridinic Nitrogen. *Angew. Chem. Int. Ed.*, **2020**, *59*, 4914-4919.
19. Cheng, Y; Veder, J. P; Thomsen, L; Zhao, S. Y; Saunders, M; Demichelis, R; Liu, C; De Marco, R; Jiang, S. P. Electrochemically Substited Metal Phthalocyanines, e-MPc (M=Co, Ni), as Highly Active and Selective Catalysts for CO_2 Reduction. *J. Mater. Chem. A*, **2018**, *6*, 1370-1375.
20. Morlanes, N; Takanabe, K; Rodionov, V. Simultaneous Reduction of CO_2 and Splitting of H_2O by a Single Immobilized Cobalt Phthalocyanine Electrocatalyst. *ACS Catal.*, **2016**, *6*, 3092-3095.
21. Aoi, S; Mase, K; Ohkubo, K; FUkuzumi, S. Selective Electrochemical Reduction of CO_2 to CO with a Cobalt Chlorin Complex Adsorbed on Multi-walled Carbon Nanotubes in Water. *Chem. Commun.*, **2015**, *51*, 10226-10228.

22. Reuillard, B; Ly, K. H; Rosser, T. E; Kuehnel, M. F; Zebger, I; Reisner, E. Tuning Product Selectivity for Aqueous CO_2 Reduction with a Mn(bipyridine)-pyrene Immobilized on a Carbon Nanotube Electrode. *J. Am. Chem. Soc.*, **2017**, *139*, 14425-14435.
23. Weng, Z; Wu, Y. S; Wang, M. Y; Jiang, J. B; Yang, K; Huo, S. J; Wang, X. F; Ma, Q; Brudvig, G. W; Batista, V. S; Liang, Y. Y; Feng, Z. X; Wang, H. L. Active Sites of Copper-complex Catalytic Materials for Electrochemical Carbon Dioxide Reduction. *Nat. Commun.*, **2018**, *9*, 415-423.
24. Wang, M; Chen, L. J; Lau, T. C; Robert, M. A Hybrid Co Quaterpyridine Complex/Carbon Nanotube Catalytic Material for CO_2 Reduction in Water. *Angew. Chem. Int. Ed.*, **2018**, *57*, 7769-7773.
25. Wu, Y. S; Jiang, Z; Lu, X; Liang, Y. Y; Wang, H. L. Domino Electroreduction of CO_2 to Methanol on a Molecular Catalyst. *Nature*, **2019**, *575*, 639–642.
26. Tornow, C. E; Thorson, M. R; Ma, S; Gewirth, A. A; Kenis, P. J. A. Nirogen-Based Catalysts for the Electrochemical Reduction of CO_2 to CO. *J. Am. Chem. Soc.*, **2012**, *134*, 19520-19523.
27. Kramer, W. W; McCrory, C. C. L. Polymer Coordination Promotes Selective CO_2 Reduction by Cobalt Phthalocyanine. *Chem. Sci.*, **2016**, *7*, 2506-2515.
28. Maurin, A; Robert, M. Noncovalent Immobilization of a Molecular Iron-Based Electrocatalyst on Carbon Electrodes for Selective, Efficient CO_2-to-CO Conversion in Water. *J. Am. Chem. Soc.*, **2016**, *138*, 2492-2495.
29. Maurin, A; Robert, M. Catalytic CO_2-to-CO Conversion in Water by Covalently Functionalized Carbon Nanotubes with a Molecular Iron Catalyst. *Chem. Commun.*, **2016**, *52*, 12084-12087.
30. Wu, Y. S; Jiang, J. B; Weng, Z; Wang, M. Y; Broere, D. L. J; Zhong, Y. R; Brudvig, G. W; Feng, Z. X; Wang, H. L. Electroreduction of CO_2 Catalyzed by a Heterogenized Zn-Porphyrin Complex with a Redox-Innocent Metal Center. *ACS Cent. Sci.*, **2017**, *3*, 847-852.
31. Mohamed, E. A; Zahran, Z. N; Naruta, Y. Efficient Heterogeneous CO_2 to CO Conversion with a Phosphonic Acid Fabricated Cofacial Iron Porphyrin Dimer. *Chem. Mater.*, **2017**, *29*, 7140-7150.
32. Pander, J. E; Fogg, A; Bocarsly, A. B. Utilization of Electropolymerized Films of Cobalt Porphyrin for the Reduction of Carbon Dioxide in Aqueous Media. *Chemcatchem*, **2016**, *8*, 3536-3545.
33. Magdesieva, T. V; Yamamoto, T; Tryk, D. A; Fujishima, A. Electrochemical Reduction of CO_2 with Transition Metal Phthalocyanine and Porphyrin Complex Supported on Activated Carbon Fibers. *J. Electrochem. Soc.*, **2002**, *149*, D89-D95.
34. Karapinar, D; Zitolo, A; Huan, T. N; Zenna, S; Taverna, D; Tizei, L. H. G; Giaume, D; Marcus, P; Mougel, V; Fontecave, M. Carbon-Nanotube-Supported Copper Polyphthalocyanine for Efficient and Selective Electrocatalytic CO_2 Reduction to CO. *Chemsuschem*, **2020**, *13*, 173-179.
35. Xia, Y. J; Kashtanov, S; Fu, P. F; Chang, L. Y; Feng, K; Zhong, J; Guo, J. H; Sun, X. H. Identification of Dual-active Sites in Cobalt Phthalocyanine for Electrochemical Carbon Dioxide Reduction. *Nano Energy*, **2020**, *67*, 104163-104168.